Check for updates

Mesoporous MnCo$_2$S$_4$ nanosheet arrays as an efficient catalyst for Li–O$_2$ batteries†

Zoya Sadighi, [iD] [a] Jiapeng Liu, [iD] [a] Francesco Ciucci [iD] [a,b] and Jang-Kyo Kim [iD] *[a]

Ternary metal sulfides and ternary metal oxides have received much attention as potential electrodes for high performance rechargeable batteries. Herein, MnCo$_2$S$_4$ nanosheets are grown on carbon paper (MCS/CP) *via* facile electrodeposition followed by low temperature vulcanization for application in Li–O$_2$ batteries for the first time. The electrochemical performance of freestanding, binder-free MCS/CP oxygen electrodes is compared with those prepared from MnCo$_2$O$_4$ nanosheets on CP (MCO/CP). The MCS/CP electrode delivers an extremely high initial specific capacity of 10 760 mA h g^{-1}, twice that of MCO/CP. The former electrode sustains 96 cycles at an upper limit capacity of 500 mA h g^{-1} at 200 mA g^{-1}, whereas the latter counterpart survives only a few cycles with a poor round trip efficiency. The superior performance of MCS/CP is in part proven by the four times higher electrical conductivity and 250% higher lithium diffusion coefficient than MCO/CP. In addition, the 3D interconnected web of 2D MCS nanosheets offers a few micrometer open voids to accommodate discharge products and a large surface area with internal mesopores providing abundant active sites. The density functional theory calculations reveal a lower adsorption energy for LiO$_2$ on the surface of MCS than on MCO, which is responsible for the lower OER overpotential and the higher catalytic ability of MCS/CP. The predicted density of states signifies metallic properties of MCS in agreement with the high electrical conductivity of MCS/CP.

Introduction

Non-aqueous lithium–oxygen batteries (LOBs) can potentially offer a high energy density of 3505 W h kg^{-1}, which is about ten times as high as that of the commercial lithium-ion batteries (LIBs).[1] Their promising specific capacity has attracted considerable interest for use in next-generation electric vehicles (EV).[2] However, the commercialization of LOBs has been severely impeded by many functional shortcomings,[3] such as their poor cycling stability, low rate capabilities, low coulombic efficiencies and high overpotentials. A major

reason behind these limitations is the sluggish kinetics of oxygen reduction and evolution reactions (ORR/OER) in the oxygen electrode.[4] In other words, developing a high performance oxygen catalyst is essential to enhance electrochemical activities during cycles.[4]

Ternary transition metal oxides, XY$_2$O$_4$ (where X = Ni, Zn and Y = Co, Fe, Mn), have superior electrochemical activities to binary metal oxides.[5] For instance, the electrical conductivity of NiCo$_2$O$_4$ is at least twice higher than that of nickel oxides or cobalt oxides.[6] These ternary metal oxides have been extensively studied for energy storage devices, especially LIBs[7] and supercapacitors.[6,8–10] Apart from ternary metal oxides, ternary metal sulfides, such as CuCo$_2$S$_4$,[11] ZnCo$_2$S$_4$[12] and NiCo$_2$S$_4$,[12–14] have also received much attention as oxygen electrodes in LOBs due to their unique two-dimensional (2D) nanosheet (NS) structure as well as their high electrical conductivity and high electrochemical stability.[15] Ni–Co sulfides possess a higher electrical conductivity than their oxide counterparts because of much lower optical bandgaps in the sulfides than the oxides have.[16] The substitution of oxygen with sulfur leads to an increase in lattice parameters and a reduction in bandgap.[17] Furthermore, transition metal sulfides are a more attractive choice than metal oxides or Si in practical battery design because the former electrodes endure significantly lower volume expansion during cycles[18] than Si electrodes that have to tolerate over 300% volume expansion.[19] In

*[a]Department of Mechanical and Aerospace Engineering, The Hong Kong University of Science and Technology, Clear Water Bay, Hong Kong, China.
E-mail: mejkkim@ust.hk*
[b]Department of Chemical and Biological Engineering, The Hong Kong University of Science and Technology, Clear Water Bay, Hong Kong

†Electronic supplementary information (ESI) available: Preparation of electrode materials, characterization, electrochemical measurements, theoretical calculations, photograph of the LOB device, electrodeposition CV curves, EDX spectra of MCS/CP, general XPS spectra, FESEM images of MCS/CP, EDX elemental maps of MCO/CP, TEM images of MCO/CP, *ex situ* XPS spectra, current–voltage (*I–V*) graphs, schematic of MCS primitive- and super-cells, *ex situ* XRD spectra of MCS/CP, CV curves of the MCO/CP and CP, table of specific surface area, pore volume, electrical conductivity, lithium diffusion coefficient, calculated surface area of MCS crystal planes, energy of three low-index surfaces, and impedance parameters calculated from the equivalent circuit. See DOI: 10.1039/c8nr03942a

terms of oxygen electrochemistry, it has been proven that metal sulfides offer a high ORR activity in fuel cells with aqueous solutions.[20] The 2D layer-structured metal sulfides consisting of loosely-stacked NSs can accommodate the volume expansion upon the storage of lithium peroxide (Li_2O_2) during ORR and mitigate the induced surface strains, leading to enhanced cycling stability.[18] There are a few successful examples of oxygen electrodes made from binary metal sulfides,[21–23] and their performances in LOBs are discussed in the next section. Notwithstanding a few studies on the synthesis of $MnCo_2S_4$ (MCS)[15,24] or $CoMn_2S_4$[25] and their applications in supercapacitors,[12,15,24,25] the current work is the first paper reporting on MCS as the electrode for lithium batteries, particularly LOBs. None of the previous studies were supported by simulations or theoretical calculations of underlying catalytic activities of the electrodes. Electrodeposition is a simple and versatile method to grow thin layers of transition metal sulfides or oxides on a substrate. In cathodic electrodeposition, the dissolved ions are driven towards the substrate to deposit on its surface with a desired morphology in a very short time.[26] The facile, low-cost electrodeposition strategy is an environmentally friendly way to produce a large amount of metal sulfides or oxides.[27] In this study, MCS NSs were

nucleated and grown on a carbon paper (CP) as the main support and gas diffusion layer (GDL) *via* cathodic electrodeposition, followed by vulcanization to stabilize the sulfide phase. The experimental conditions and characterization details are presented in the ESI.† The electrochemical performance of the MCS/CP cathode in a custom-built LOB cell (Fig. S1†)[28–30] was measured and compared with that of the cathode prepared from $MnCo_2O_4$ NSs grown on CP (MCO/CP). The density functional theory (DFT) calculations based on first principles were employed to verify the more rigorous catalytic activities and thus much higher discharge capacities of the MCS/CP electrode than those of MCO/CP.

Results and discussion

Characterization of materials and structure

Fig. 1a illustrates the procedure used for the growth of MCS NSs on CP (MCS/CP). Mn–Co-sulfate NSs were cathodically grown on CP through the electrochemical redox reaction, in which anion exchanges simultaneously occurred between Mn, Co precursors and S^{2-} anions.[25] The Mn–Co-sulfate NSs (Fig. S2†) were vulcanized to form mesoporous MCS NS arrays
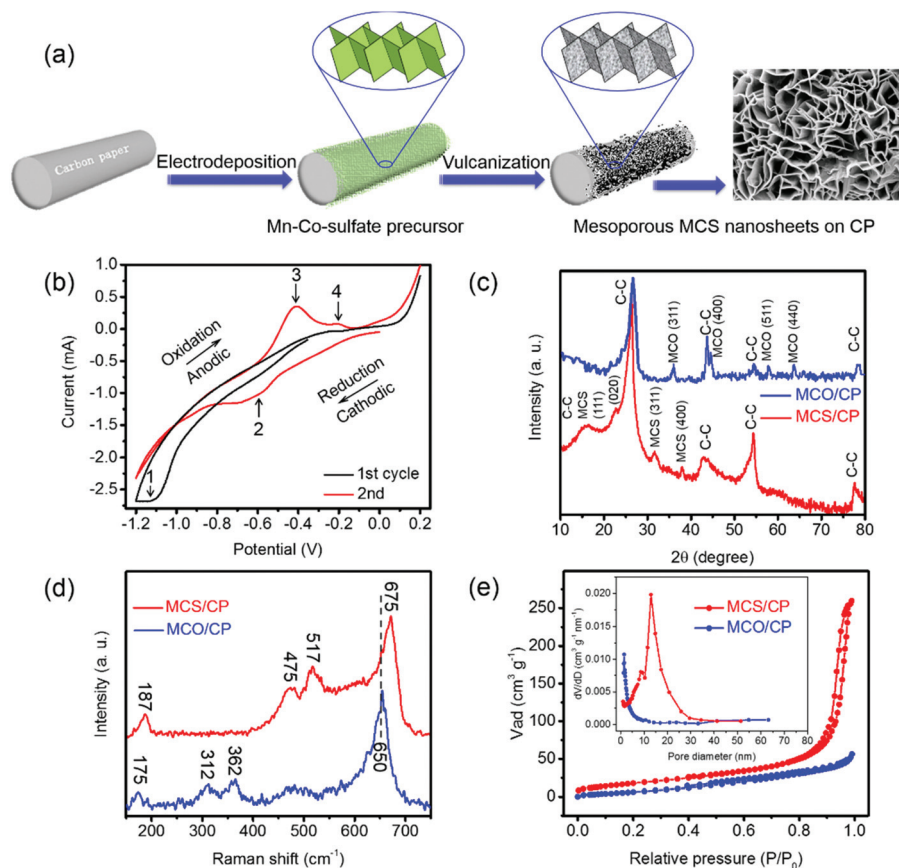
Fig. 1 (a) Illustration of the synthesis procedure and (b) the first two cycles of CV curves in the electrodeposition process of MCS nanosheets on CP. Comparison of (c) XRD spectra, (d) Raman spectra, (e) N_2 adsorption/desorption isotherm curves and (inset in e) pore size distributions of MCS/CP and MCO/CP.

on the CP support at 180 °C, see the ESI.† The cyclic voltammetry (CV) curves of the first two cycles of electrodeposition are shown in Fig. 1b. Various steps of NS growth are explained as follows. (i) In the first cathodic sweep, the peak at ~−1.1 V (Arrow 1) is related to the functionalization of CP to generate oxygenated functional groups, such as COOH, CO and OH.[31] (ii) In the second cycle and onwards, there were one reduction peak in the cathodic sweep at ~−0.6 V (Arrow 2), and two distinct oxidation peaks in the anodic sweep, at ~−0.4 (Arrow 3) and −0.2 V (Arrow 4). The reduction peak at ~−0.6 V is ascribed to the electroreduction of thiourea and the formation of MCS NSs.[32] The anodic peaks at ~−0.4 and −0.2 V are related to the oxidation and deposition of Co and Mn precursors, respectively.[26,27] Fig. S3† shows the corresponding CV curves in the following cycles. It is of interest to note that the Co oxidation peaks shifted toward the Mn oxidation peaks with increasing cycles, signifying the preferential deposition of Co against Mn and the removal of electrodeposited Mn during the first cycle when the Co concentration increased.[26] The preferential deposition of Co was attributed to the hydroxide suppression mechanism (HSM) in which the pH value of the as-deposited CP surface increased due to the hydrogen evolution. The elevated pH resulted in the formation of Co hydroxide on the surface which acted as a selective membrane to decrease Mn deposition upon further cycles.[32–34] The Co/Mn and S/(Mn + Co) atomic ratios, ~1.9 and ~1.3, respectively, measured by energy dispersive X-ray spectroscopy (EDX, Fig. S4†), reflect the stoichiometric $MnCo_2S_4$ composition in the bulk MCS. The Co/Mn atomic ratio on the surface was almost the same as in the bulk, ~1.8, according to X-ray photoelectron spectroscopy (XPS, Fig. S5†). The lower S/(Mn + Co) ratio, ~0.2, of the surface probably arose from the surface oxidation.

The X-ray diffraction (XRD) pattern of MCS/CP (Fig. 1c) presents prominent peaks at ~27°, 43°, 55° and 78° which are also shared with MCO NSs. Two sulphospinel peaks located at 27° and 55° are the superposition of the CP dominant peaks. The peak at 22.5° is related to the (020) reflection of metal sulfate, representing the surface oxidation of MCS which is also reflected by the oxygen peaks in the XPS spectra (Fig. S5†).[14,24,25] Broad peaks with low intensities also appeared at $2\theta = 31.5°$ and 38.3°, which arose from the (311) and (400) planes corresponding to the sulphospinel structure.[12,24] The formation of $MnCo_2S_4$ composition in the bulk of MCS/CP was assured with the appearance of the sulphospinel peaks. The XRD spectrum of MCO/CP revealed peaks at ~36°, 43.7°, 58°, and 63.5° corresponding to the (311), (400), (511), and (440) planes of $MnCo_2O_4$, JCPDS no. of 23-1237. The Raman spectrum of MCS NSs (Fig. 1d) presents four peaks centered at ~187, 475, 517 and 675 cm⁻¹ which correspond to the Co–S bonds, the E_g stretching mode of Co–S vibration,[25,35] the Mn–S bonds[25] and the A_{1g} symmetry of Co–S, respectively.[25,35] In the Raman spectrum of MCO NSs, the peaks related to the metal sulfur bonds disappeared, while two distinct peaks at ~312 and 362 cm⁻¹ appeared indicating the Mn–O bonds. The sharp peaks at ~175 and 650 cm⁻¹ are ascribed to the Co–O bonds and vibrational mode of oxygen

atoms in the octahedral sites,[29] respectively. These peaks were down-shifted from ~187 and 675 cm⁻¹ for MCS NSs, reflecting the substitution of sulfur in the spinel structure with oxygen.[17,24]

The N_2 adsorption/desorption isotherm and pore size distribution curves (Fig. 1e) indicate a highly mesoporous structure of MCS NSs. The isotherm curve had a hysteresis loop of Type IV with mainly a mesoporous structure. However, the MCO NSs showed a Type I isotherm with saturation at a low relative pressure (P/P_0) of 0.4 holding a majority of micropores and a small percentage of mesopores.[36] The MCS NSs possessed a much larger specific surface area and a larger pore volume of 65.4 m² g⁻¹ and 0.41 cm³ g⁻¹, respectively, than 27.4 m² g⁻¹ and 0.083 cm³ g⁻¹ for MCO NSs (Table S1†). These mesopores with sizes ranging from 2–30 nm (Fig. 1e inset) are particularly useful as pathways for fast ion-transport,[37] effectively contributing to the enhancement in discharge capacity.[38] In contrast, most pores of the MCO NSs were smaller than 5 nm having a relatively low impact on catalytic activity or mass transportation.[38] In particular, the micropores are easily blocked by Li_2O_2 so that the surface area of these pores would not be available for electrochemical reactions.[39]

The field emission scanning electron microscopy (FESEM) images (Fig. 2a and d) of pristine CP present a smooth surface of carbon fibers with diameters ranging from 6–7 μm. The macroscale empty space between the individual fibers facilitated the movement of O_2 while the electrons were transported along the carbon fibers.[38] Fig. 2b and e present the corresponding images of MCS NSs which were grown nearly perpendicular to the surface of carbon fibers (Fig. S6a†). They formed a continuous coating along the whole fiber length with a moderately uniform thickness. The average thickness of the individual MCS NSs was about 4 μm (Fig. S6b†), much larger than that of MCO NSs (Fig. 2c and f), leading to a larger surface area of the former electrode (Table S1†). The larger open voids among MCS NSs (Fig. 2e and S6a†) than MCO NSs (Fig. 2f) may offer enough space to accommodate the accumulation of discharge products (Li_2O_2) during ORR.[18,38] The large open voids also enhanced the wettability of 3D MCS NSs and carbon fibers by the electrolyte. It follows then that the mesopores along the NSs provide the required active sites for ORR.[38] Furthermore, the binder-free cathode can avoid its negative effects: for example, binders may block the pores smaller than 30 nm in width, effectively reducing the surface area and pore volume causing lower ORR activities.[40] The EDX elemental maps of MCS (Fig. 2g) and MCO (Fig. S7†) NSs confirmed the homogeneous distribution of Mn, Co, and S, or O, along the fiber surface. The elemental maps exhibit a higher Co content than Mn in agreement with the observations from Fig. 1b and S3.†

The transmission electron microscopy (TEM) images of MCS NSs depict high contrast between the background and overlapped dark walls reflecting the size of open voids ranging from several hundred to few thousand nanometers in width (Fig. 2h and i inset), consistent with the SEM images (Fig. 2e and S6a†). The high resolution TEM (HRTEM) images (Fig. 2i
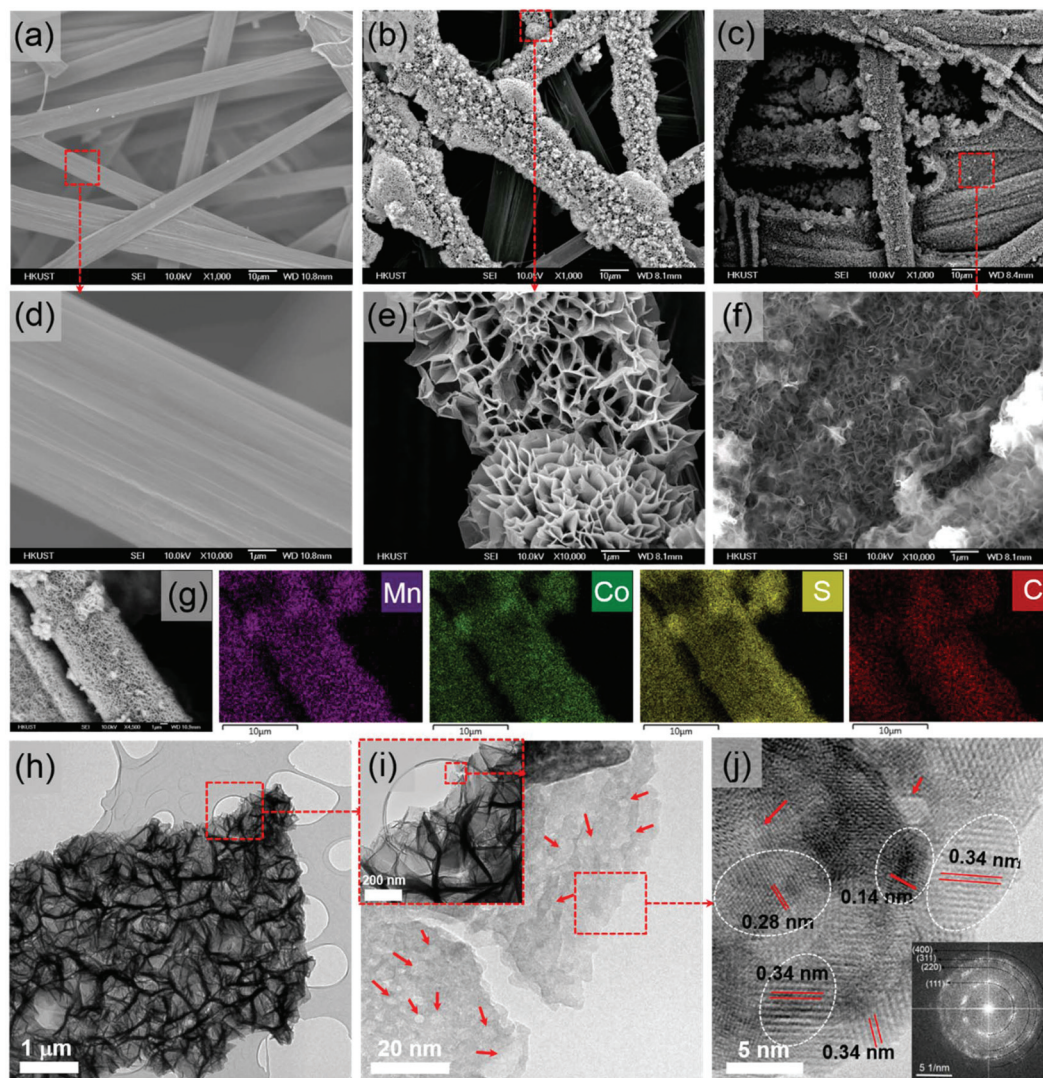
Fig. 2 FESEM images of (a, d) pristine CP, (b, e) MCS/CP and (c, f) MCO/CP taken at low and high magnifications; (g) EDX elemental maps of MCS/CP. (h–j) TEM and HRTEM images of electrodeposited MCS NSs on CP. Red arrows show internal mesopores in (i) and (j). The FFT pattern is shown as inset of (j).

and j) show internal mesopores in MCS NSs, as indicated by arrows, which stemmed from the replacement of O^{2-} by S^{2-} during vulcanization.[24] In contrast, the same magnification HRTEM images of MCO (Fig. S8b†) showed plain NSs without a mesoporous structure. The MCS NSs were composed of nanocrystals with very fine crystal sizes of less than 10 nm, see white dotted circles in Fig. 2j. The fringe lattices and distinct diffraction rings shown by the fast Fourier transform (FFT) pattern (in inset) indicate their polycrystalline nature. The inter-planar distances of 0.34, 0.28 and 0.14 nm are ascribed to the (220), (311) and (533) crystallographic planes related to the sulphospinel structure, in agreement with JCPDS no. 43-1477 for a nickel–cobalt sulphospinel.[24,41] The d-spacing of 0.34 nm was chosen for the calculation of adsorption energies using the DFT analysis. The HRTEM image for MCO NSs (Fig. S8c†) revealed the (311) and (440) planes with inter-

planar distances of 0.25 and 0.15 nm, respectively, reflecting the formation of $MnCo_2O_4$ (JCPDS no. 23-1237).

The general XPS spectra (Fig. S5†) reveal a higher Co concentration than Mn in both MCS/CP and MCO/CP. The C 1s peak in the general scan belongs to CP. A comparison between the spectra of the two composite electrodes clearly indicates a prominent peak of S 2p (Fig. S5†) in the former electrode and the O 1s peak with a much higher intensity in the latter. The O 1s peak in MCS/CP is ascribed to the surface oxidation due to the exposure to air.[14,24,32] However, neither the $MnCo_2O_4$ peak nor metal–oxide bonds were detected in the XRD spectrum of MCS/CP (Fig. 1c) and the corresponding Raman (Fig. 1d) spectrum. Therefore, in view of the very shallow probe depth (≤5 nm) of XPS analysis, it is affirmed that the very top surface layer on MCS contained oxide, while its bulk was made of sulfide $MnCo_2S_4$, as shown by the XRD spectrum (Fig. 1c). The
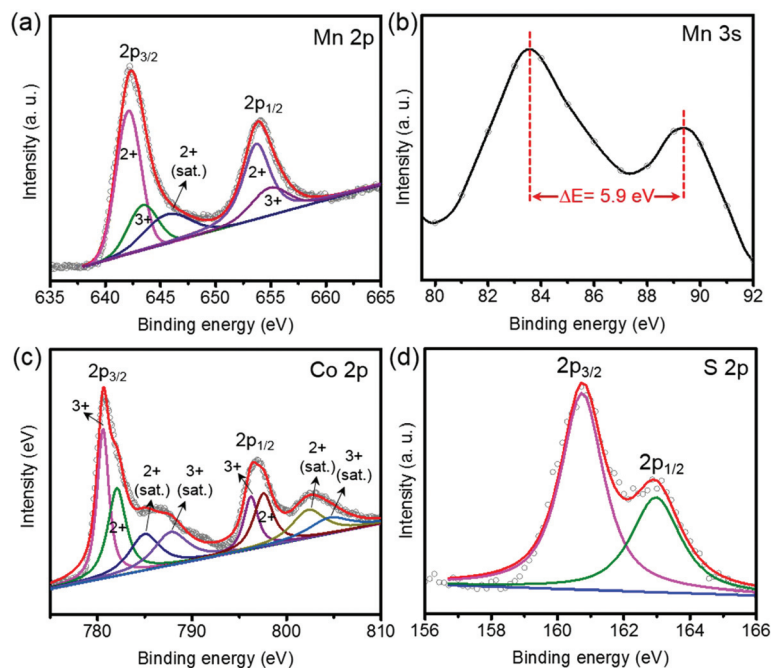
**Fig. 3** XPS spectra with deconvoluted peaks of (a) Mn 2p, (b) Mn 3s, (c) Co 2p and (d) S 2p for MCS/CP.

high resolution spectra with deconvoluted peaks of Mn 2p, Mn 3s, Co 2p and S 2p for MCS/CP are given in Fig. 3. Two spin orbit doublets of Mn $2p_{3/2}$ and Mn $2p_{1/2}$ are located at 642.3 and 653.9 eV with an energy separation of 11.6 eV (Fig. 3a), reflecting the dominance of Mn^{2+} ions.[24] A satellite at 645.6 eV is another piece of evidence of Mn^{2+} valence.[42] The deconvoluted Mn 2p is fitted with four peaks corresponding to Mn^{2+} at 642.1 and 653.7 eV; and Mn^{3+} at 643.4 and 654.9 eV. The Mn valence is better reflected by the Mn 3s exchange splitting energy, $\Delta E = \sim 5.9$ eV, indicative of the 2+ ionic state of Mn (Fig. 3b).[43] The energy separation between Co $2p_{3/2}$ (at 780.6 eV) and Co $2p_{1/2}$ (at 796.8 eV) in the Co 2p spectrum (Fig. 3c) was 16.2 eV, verifying the co-existence of Co^{2+} and Co^{3+}.[14,24] After deconvolution, Co 2p presents four major peaks at 780.6, 796.2 eV and 782.0, 797.5 eV which are attributed to Co^{3+} and Co^{2+} ions, respectively, along with 3+ (787.7 and 804.5 eV) and 2+ (785.0 and 802.3 eV) shakeup satellite peaks. The less dominant satellites reflect the presence of mixed Co^{2+} and Co^{3+} oxidation states.[25] For S 2p (Fig. 3d), two peaks were observed at 160.7 and 163.0 eV, corresponding to the S $2p_{3/2}$ and S $2p_{1/2}$, respectively.[35,44] These two peaks are typical of metal–sulfur bonds in the ternary metal sulfides, in agreement with the cobalt sulfide and manganese sulfide binding energies.[14,25,35,44,45]

Electrochemical performance

The electrochemical performances of different electrodes are shown in Fig. 4. The MCS/CP electrode delivered a first discharge capacity of 10 760 mA h g^{-1} (Fig. 4a), more than twice 4970 mA h g^{-1} for MCO/CP and much higher than 1200 mA h g^{-1} for the pristine CP. The discharge plateau of the former

electrode was higher by over 100 mV than those of the other two electrodes, whereas its charge plateau was much lower by 500 and 950 mV, respectively, than those of the latter two electrodes (Fig. 4a). The MCS NS catalyst decreased the overpotential of CP throughout the potential range which was taken at 250 mA h g^{-1}, which is half the upper-limit capacity given in Fig. 4b. The ORR overpotential was reduced from 1.1 to 0.51 V, while the OER overpotential was reduced from 0.42 to 0.31 V. However, marginally lower charge and discharge overpotentials were recorded for MCO/CP relative to CP. These observations reflect the enhanced capability of MCS NSs to reduce O_2 during ORR and to decompose the discharge products during OER with a markedly higher energy efficiency than MCO NSs and pristine CP. The round-trip energy efficiency of the MCS/CP cathode at an upper limit capacity of 500 mA h g^{-1} was 76.5%, which compares well with 77% for the expensive PtAu/C cathode.[46] The round-trip efficiencies of the MCO/CP and CP cathodes under the same conditions were 65.5% and 62.7%, respectively.

The long-term cycling stabilities of these electrodes examined at 200 mA g^{-1} with an upper-limit capacity of 500 mA h g^{-1} are shown in Fig. 4c–h. The MCS/CP electrode survived 96 cycles at the upper-limit capacity (Fig. 4c and d). The sharp increase in charge potential of MCS/CP during the first 10 cycles might be related to the passivation of bare sides of CP due to the formation of Li_2CO_3 requiring a higher voltage to decompose compared to Li_2O_2.[47] On the other side, the MCO/CP survived only 11 cycles with a poor coulombic efficiency of 92%. Although this electrode could be charged to 500 mA h g^{-1} for 40 cycles, it was unable to complete the ensuing discharge process for most cycles (Fig. 4e and f). The charge voltage of
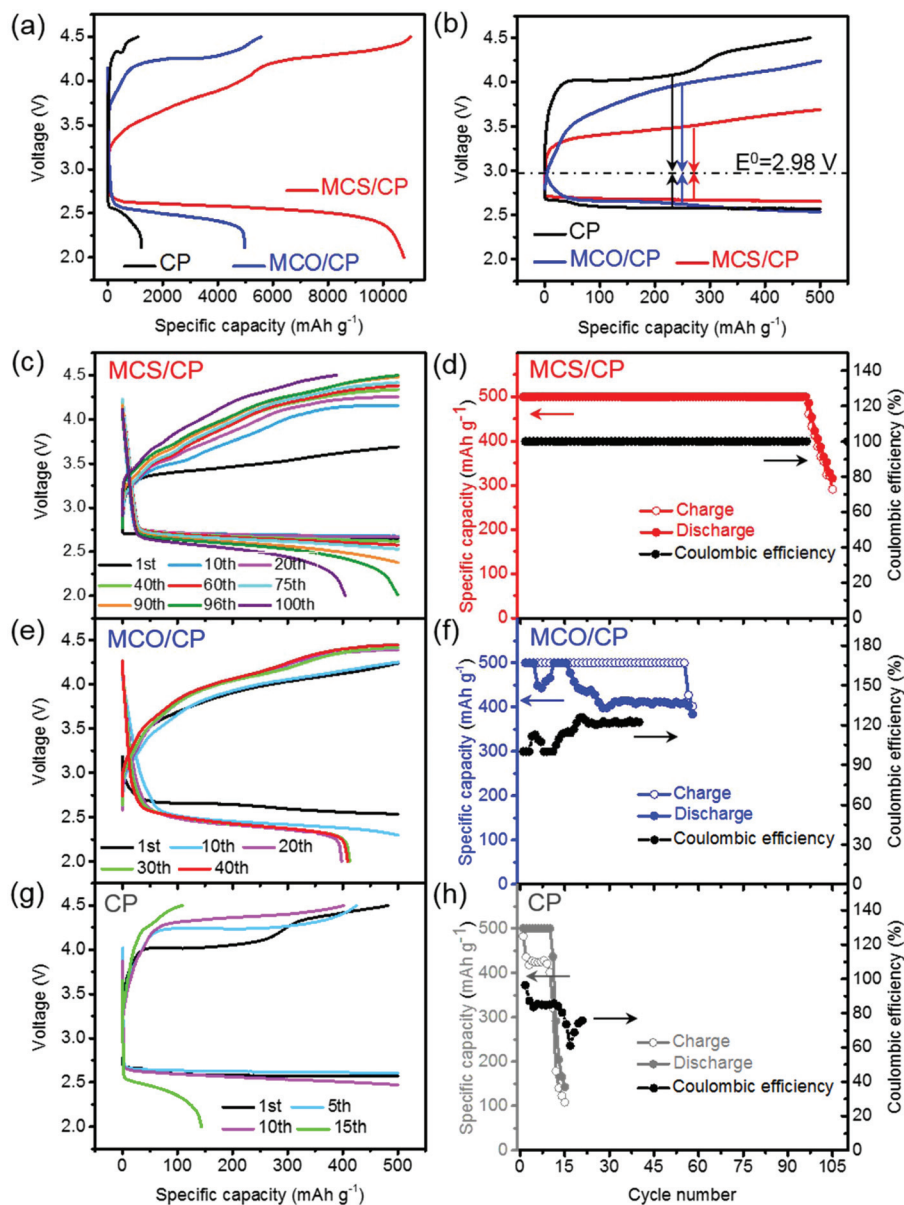
Fig. 4 Comparison of discharge/charge curves of LOBs with MCS/CP, MCO/CP and pristine CP cathodes at a current density of 200 mA g^{-1} (a) for the full capacity and (b) with an upper-limit capacity of 500 mA h g^{-1}. Discharge/charge curves at different cycles, cycling performance with an upper limit capacity of 500 mA h g^{-1} and coulombic efficiency of (c, d) MCS/CP, (e, f) MCO/CP and (g, h) CP.

the electrode increased beyond 4.3 V only after 10 cycles (Fig. 4e), leading to the decomposition of the electrolyte, accumulation of insulating RCOOLi and Li$_2$CO$_3$ on the cathode surface and reduced concentration of Li$^+$ ions in the electrolyte.[29] The presence of these reaction products will be further discussed with the *ex situ* XPS analysis (Fig. S9†). The pristine CP electrode was only stable for a few cycles because it failed to recover the discharge capacity when charged to 4.5 V (Fig. 4g and h), also evidenced by the poor coulombic efficiency (Fig. 4h). The superior cycling performance of the MCS/CP electrode is partly attributed to its higher electrical conductivity. Fig. S10† shows the current–voltage (I–V) graphs of MCS/CP and MCO/CP obtained by the Hall/resistivity

measurements, confirming a much higher electrical conductivity of MCS/CP than MCO/CP (Table S1†).

Fig. 5 shows the comparison of electrochemical performance of the MCS/CP and MCO/CP cathodes with those of transition metal sulfide- and oxide-based electrodes reported in the literature.[21–23,48,49] The oxygen electrode made of a Co$_3$S$_4$ NS catalyst and Ketjenblack (KB) (1 : 2) delivered 5917 mA h g^{-1} at 100 mA g^{-1} and survived 25 cycles at 500 mA h g^{-1} with ~0.9 V overpotential and a 72% round-trip efficiency.[21] The electrode prepared from a flower-like NiS (f-NiS) catalyst, super P and polyvinylidene fluoride (PVDF) at a weight ratio of 3 : 6 : 1 showed 9064 mA h g$_{cat.}^{-1}$ (cat. refers to catalyst) at 400 mA g$_{cat.}^{-1}$. The electrode was discharged for 30 cycles until the capacity
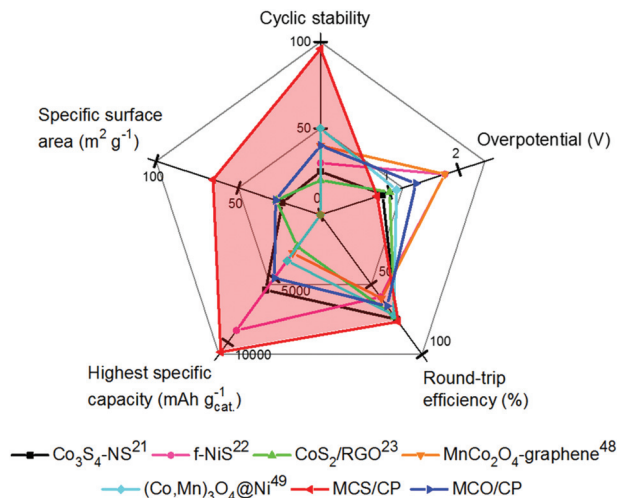
Fig. 5 Comparison of electrochemical performance of MCS/CP and MCO/CP cathodes with similar electrodes reported in the literature. The highest specific capacities are calculated based on the weight of the catalyst.

reached 1800 mA h $g_{cat.}^{-1}$ at 400 mA $g_{cat.}^{-1}$ with an overpotential of ~1.8 V and a round-trip efficiency of 59%.[22] About 78 wt% CoS_2 nanoparticles distributed on reduced graphene oxide (CoS_2/RGO) sheets were used as active catalysts in a total weight of 0.8–1 mg cm^{-2} for the oxygen electrode which showed a first discharge capacity of ~2500 mA h $g_{cat.}^{-1}$ at 100 mA $g_{cat.}^{-1}$ and survived 20 cycles at 200 mA $g_{cat.}^{-1}$ with an overpotential and a round-trip efficiency of 1 V and ~73%, respectively.[23] The $MnCo_2O_4$–graphene catalyst with a 0.5 mg cm^{-2} loading had a discharge capacity of ~3000 mA h $g_{cat.}^{-1}$ at 400 mA $g_{cat.}^{-1}$ and survived 40 cycles at a cut-off capacity of 1000 mA h $g_{cat.}^{-1}$.[48] The 2–3 mg (Co, Mn)$_3O_4$ nanowire electrode grown on a Ni foam of 12 mm in diameter showed a first discharge capacity of 3605 mA h $g_{cat.}^{-1}$ at 100 mA $g_{cat.}^{-1}$ with a round-trip efficiency of 72% and an overpotential of 1.1 V. It survived 50 cycles at a cut-off capacity of 500 mA h $g_{cat.}^{-1}$.[49] The summary radar chart (Fig. 5) reveals that the MCS/CP electrode outperformed other electrodes in terms of all categories shown, including cycling stability, specific capacity, specific surface area, overpotentials and round-trip efficiency.

To support the outperformance of the MCS/CP electrode compared to the MCO/CP counterpart, we studied the electronic density of states (DOS) of the two electrodes using DFT. The primitive- and super-cells of MCS are illustrated in Fig. S11a and b,† respectively, where the Mn atoms occupy the tetrahedral sites and the Co atoms occupy the octahedral sites. A lattice constant of 9.641 Å was obtained for the MCS supercell (Fig. S11b†), whereas the substitution of S with O to form the MCO cell reduced the lattice constant to 8.205 Å.[17] The total and partial electronic densities of states for MCS and MCO were calculated, as shown in Fig. 6a. MCS exhibited a metallic behavior due to the lack of bandgap in both spin-up and spin-down channels, whereas MCO presented a semiconducting behavior with discontinuous energy bands near the

Fermi level in the spin-down state. A bandgap of 0.65 eV for MCO suggests a poorer electron transport ability in oxides than in sulfides, consistent with the electrical conductivity measurements (Fig. S7 and Table S1†) and the electrochemical impedance spectroscopy (EIS) results (Fig. 8a and b).[28,30,50]

To evaluate the binding energies between the species, Li_2O_2, LiO_2 and O_2, and the catalyst, the surface energies of three low-index surfaces of MCS were studied based on the DFT calculations.[51,52] Table S2† shows that the lowest energy belongs to the (110) plane, in agreement with the HRTEM observations. Therefore, a focused study was done of the (110) plane to evaluate the adsorption energies in the LOB system. Before calculating the adsorption energies, the (110) plane slab (Fig. 6c) was optimized and relaxed, resulting in reconstruction of the atoms, especially the Mn atoms, on the surface shown in Fig. 6d. When the Li atoms were added, they preferably adsorbed onto the Co sites.[53] Then by addition of the oxygen molecules, the strong affinity of Li_2O_2 to the (110) surface of MCS with a binding energy of −5.35 eV was responsible for the enhanced discharge capacity of the MCS/CP electrode. When the Li_2O_2 or LiO_2 clusters were adsorbed onto the surface, the Mn atoms nearest them moved to the Li atoms (Fig. 6e and g). In the charge difference plot (Fig. 6f and h), the electrons were redistributed at the Li–O bond and the Mn atoms were located on the top surface. While the electrons moved from Li to O atoms, the Mn atoms also shared some electrons with O atoms, *i.e.* the orange region between the Mn and O atoms, indicating that the Li–O bond was ionic and the Mn–O bond was covalent.

One possible path for decomposition of deposited Li_2O_2 during OER is (−Li$^+$ → −Li$^+$ → −O$_2$) in which the first Li$^+$ and the second Li$^+$ and one O$_2$ molecule escape in sequence from Li_2O_2.[54,55] The reaction free energies of different steps according to the OER path from MCS and MCO (see eqn (S3)†) are shown in Fig. 6b. The generally lower energy barriers for the MCS surface than the MCO surface in Steps (1) and (2) strongly correlated with the significantly lower OER overpotential and the higher catalytic activity of the former electrode.[56] Furthermore, the desorption of O$_2$ in Step (3) is the rate-determining step in the OER path.[54] The corresponding energy barriers were much lower for MCS (1.52 eV) than MCO (3.25 eV), again reflecting a better OER activity of the former electrode. Moreover, it is reported that if the adsorption energy of LiO_2 decreased, the OER overpotential of the metal surface reduced and the catalytic activity increased.[56] The predicted adsorption energies of LiO_2 on the MCS and MCO surfaces were −3.53 and −5.74 eV, respectively, signifying a higher catalytic activity of the former electrode due to the reduced OER overpotential. These computational findings were conclusive as supported by experimental results that showed lower overpotentials and longer cycling stability for the MCS-based cathode than the MCO counterpart (Fig. 4a–f).

Ex situ characterization after cycles

Fig. 7 presents the changes in morphology of the two cathodes after 40 cycles. The MCS/CP electrode after the 40th discharge
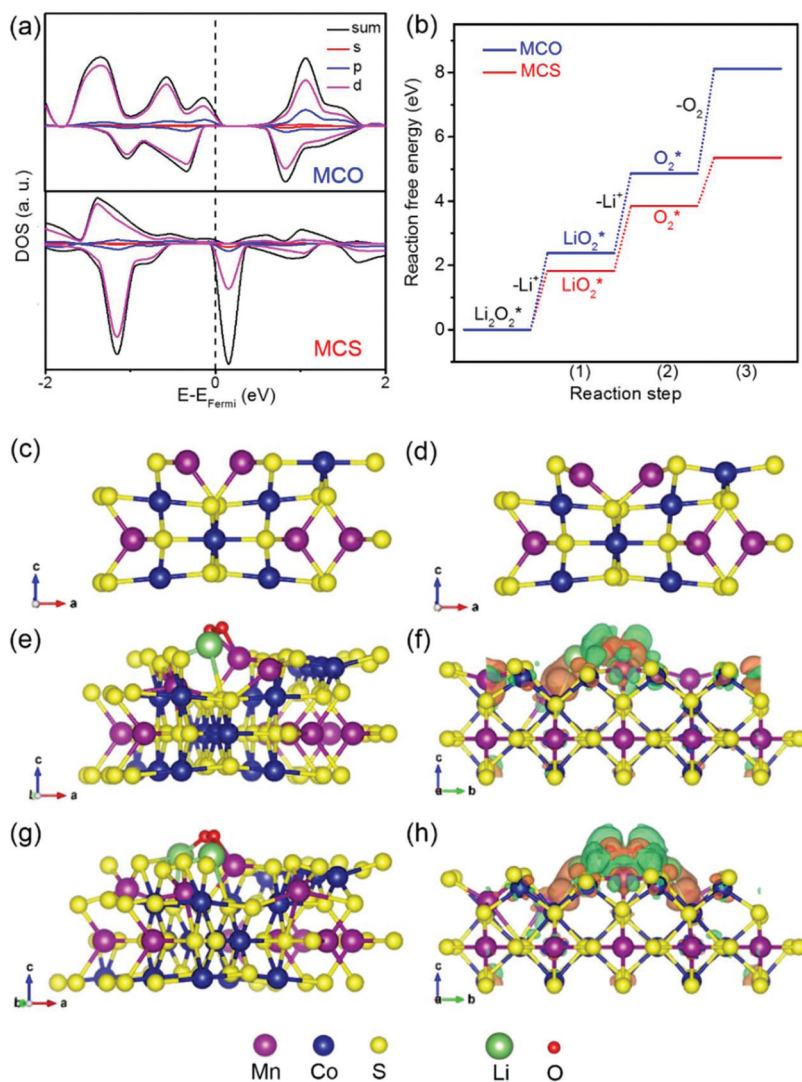
Fig. 6 (a) Total and partial electronic DOSs calculated for MCS and MCO. (b) Reaction free energies for decomposition of Li_2O_2 from the MCS and MCO surfaces according to the ($-Li^+ \rightarrow -Li^+ \rightarrow -O_2$) path: asterisks refer to the surface-adsorbed species. The MCS-(110) surface slab model (c) before and (d) after optimization and relaxation. Adsorption of (e) LiO_2 and (g) Li_2O_2; and charge difference plots of (f) LiO_2 and (h) Li_2O_2 on the (110) surface of MCS. In the charge difference plots, orange and green regions indicate positive (charge accumulation) and negative (charge depletion) domains, respectively.

(Fig. 7a) showed NSs covered with a thick layer and large particles of discharge products consisting of Li_2O_2, Li_2CO_3 and RCOOLi (see Fig. S9a†). The formation of these products was also confirmed by *ex situ* XRD analysis. After the 40th discharge (Fig. S12†), the peaks at 35, 40.5 and 58.6° reflect the (101), (102) and (110) planes of Li_2O_2 (JCPDS no. 09-0335)[29] and the ones at 23.5, 29.4 and 31.7° are related to the (200), (111) and (002) planes of Li_2CO_3 (JCPDS no. 87-0729). After the 40th charge (Fig. S12†), the Li_2O_2 and Li_2CO_3 peaks vanished, indicating complete decomposition of discharge products with highly reversible cycling stability, consistent with the disappearance of large particles from the cathode surface (Fig. 7a). The 3D reticulated structure consisting of 2D MCS NSs in the MCS/CP cathode was fully recovered after charge. For MCO/CP (Fig. 7b), in contrast, the open voids within the

NSs were filled with a thick layer of insulating discharge products after discharge, resulting in diminution of electrical conductivity, Li^+ diffusivity and O_2 reduction. The thick insulating layer failed to decompose during the charge cycle (see Fig. S9b†).

The nature of discharge products and their formation/decomposition were probed by *ex situ* XPS analysis of the cathodes, as shown in Fig. S9.† The deconvoluted Li 1s spectra after the 40th discharge presented the formation of reaction products, Li_2O_2 (54.8 eV), Li_2CO_3 (55.4 eV) and RCOOLi (56.0 eV), on both electrodes. After the 40th recharge, Li_2O_2 on the MCS/CP electrode (Fig. S9a†) decomposed with its peak completely disappearing, while the same peak for MCO/CP (Fig. S9b†) remained with a reduced intensity. The insulating lithium carbonate phase, RCOOLi and Li_2CO_3 were generated
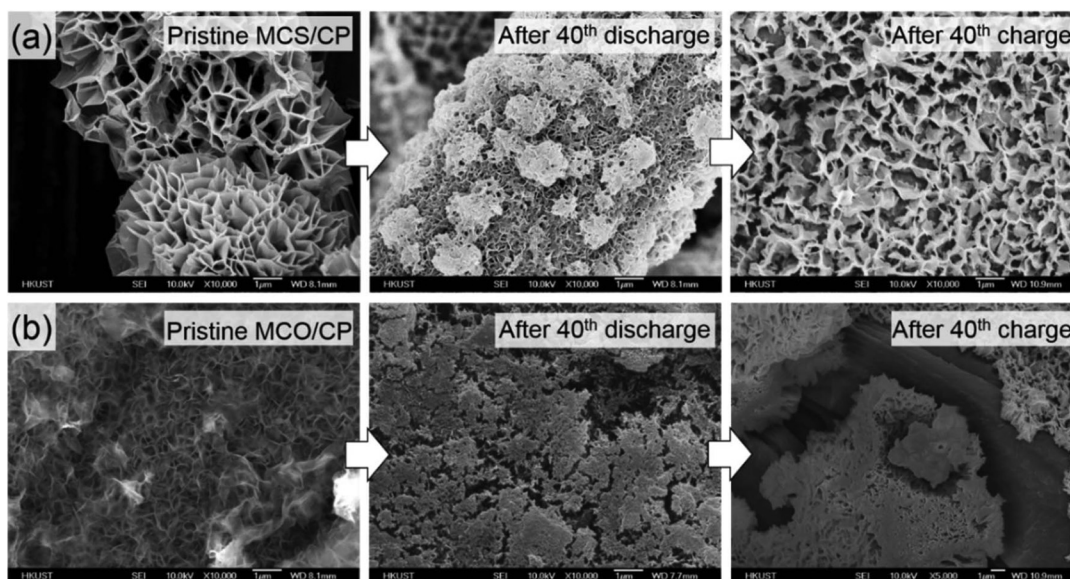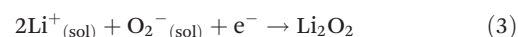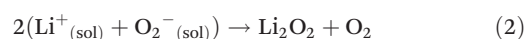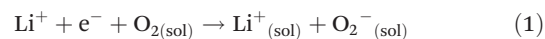
Fig. 7 *Ex situ* SEM images of (a) MCS/CP and (b) MCO/CP electrodes taken before and after the 40th discharge and charge tested at 200 mA g^{−1} at an upper-limit capacity of 500 mA h g^{−1}.

from the decomposition of a TEGDME electrolyte solvent and the oxidation of CP surface,[57,58] clogging the MCO/CP open voids (Fig. 7b), which in turn blocked the ionic diffusion pathways and significantly decreased the electrical conductivity.

In light of the above experimental findings, the mechanisms of oxygen electrochemistry can be summarized as follows. Previous studies reported[1,59–62] that at a high overpotential, O_2 was reduced to grow a discharge product film, Li_2O_2, in agreement with our observations for the MCO/CP electrode (Fig. 4a, b and 7b). At a low overpotential, however, both the film- and particle-shaped Li_2O_2 products were formed, consistent with the MCS/CP electrode (Fig. 4a, b and 7a).[59,61] The particle-shaped Li_2O_2 grew *via* a solution mechanism due to the high solubility of the LiO_2 intermediate phase. In contrast, the film-shaped Li_2O_2 was formed through a surface-dominant mechanism of low soluble LiO_2.[61,62] In other words, whether Li_2O_2 forms particles or a film was controlled by the solubility of LiO_2, depending on many factors, *e.g.* donor ability of the solvent, effective current density and overpotential.[1,60,61] Therefore, it can be concluded that at a low overpotential, the increased solubility of LiO_2 tends to form more particulate Li_2O_2.[1,59–62] In this study, MCS/CP with a significantly lower overpotential than MCO/CP showed a higher tendency to grow particle-shaped discharge products (Fig. 7b). In addition, the lower LiO_2 adsorption energies of MCS than MCO also served as evidence for the enhanced solvation of LiO_2 in the electrolyte, promoting the growth of particle-shaped Li_2O_2.[56] Eqn (1)–(3) summarize the mechanisms of forming Li_2O_2. At a low overpotential, LiO_2 is formed after O_2 is reduced by one electron (eqn (1)), an equilibrium being displaced between the surface-adsorbed LiO_2* and LiO_2 dissolved in the electrolyte. Then, LiO_2 disproportionates to Li_2O_2

and O_2 (eqn (2)) or undergoes a second reduction (eqn (3)) to form either Li_2O_2 particles or a Li_2O_2 film.[1,60,63]

$$Li^+ + e^- + O_{2(sol)} \rightarrow Li^+{}_{(sol)} + O_2{}^-{}_{(sol)} \tag{1}$$

$$2(Li^+{}_{(sol)} + O_2{}^-{}_{(sol)}) \rightarrow Li_2O_2 + O_2 \tag{2}$$

$$2Li^+{}_{(sol)} + O_2{}^-{}_{(sol)} + e^- \rightarrow Li_2O_2 \tag{3}$$

The EIS spectra for both the MCS/CP and MCO/CP electrodes were examined after cycles (Fig. 8a and b) and the impedance parameters were analyzed using the Zview software to fit equivalent circuits (Table S3†).[64] The ionic resistance of the electrolyte, R_s, for the MCO/CP cathode increased consistently with cycles due to increasingly lower Li^+ concentrations in the electrolyte resulting from the surface-adsorbed LiO_2 during discharge and the electrolyte instability.[1] This finding corroborates the increase in OER overpotential (Fig. 4e) leading to the reduction in energy efficiency. Although the initial R_s value of MCS/CP was only marginally higher than that of MCO/CP, it did not noticeably increase after 40 cycles, reflecting a higher stability of the electrolyte in contact with the metal sulfide catalyst than with the metal oxide. The fresh MCS/CP electrode presented a considerably lower charge transfer resistance, R_{ct}, than MCO/CP (Table S3†) because of the higher electrical conductivity of MCS NSs than MCO NSs (Table S1†) which was also proven by the DOS showing a metallic characteristic of MCS (Fig. 6a). The formation of insulating discharge products on the cathode surface increased the R_{ct} for both electrodes after the 1st discharge. It is worth noting that the R_{ct} value of MCS/CP almost halved upon recharge after the 40th cycle because of enhanced redox kinetics, as discussed below. The corresponding R_{ct} value of the MCO/CP electrode, however, sig-
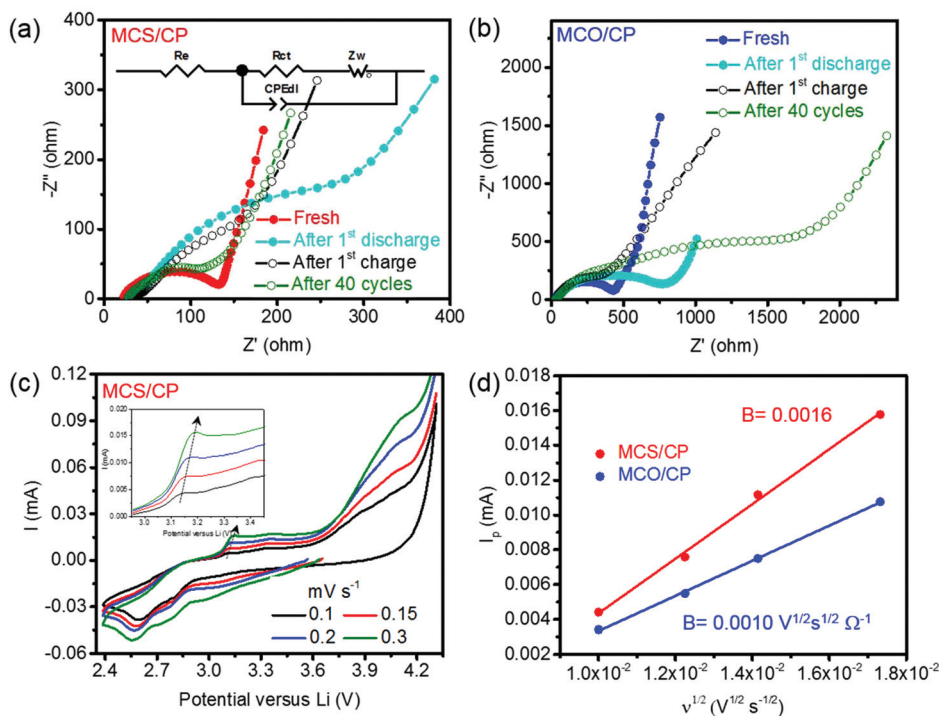
Fig. 8 EIS spectra of (a) MCS/CP and (b) MCO/CP electrodes obtained before and after one and 40 full cycles (with the equivalent circuit shown as inset in (a)); (c) CV curves of the MCS/CP electrode obtained in the third cycle at different scan rates of 0.1, 0.15, 0.2, 0.3 mV s^{-1}; and (d) anodic peak current, I_P, versus square root of scan rate, $\nu^{1/2}$.

nificantly increased after 40 cycles, by more than five times the initial value, signifying typically poor cycling performance of the cell (Fig. 4e and f). The CPE_{dl} values of the MCS/CP electrode were generally much higher than those of the MCO/CP counterpart, representing higher capability of the metal sulfide to store capacitance than the metal oxide. The continuous rise in capacitance of the MCS/CP electrode stemmed from the charges stored during the reversible redox reactions that overlapped with the charge stored from double layer capacitance of carbon fibers in CP (Fig. 2a and d). The generally much lower Z_w for MCS/CP than for MCO/CP reflects the dominant mass transport of the former electrode, resulting in fast Li$^+$ ion diffusion across the interface between the MCS catalyst and Li$_2$O$_2$. The better Li$^+$ ion diffusivity through the metal sulfide NSs than the metal oxide NSs is discussed in the following.

Kinetics of the oxygen electrochemical process

The kinetics of the oxygen electrochemical process in the LOB cell was studied using the CV curves. The oxygen electrode often undergoes an electro-activation process in the first cycle due to non-uniform distribution of oxygen throughout the bulk electrode.[62] Thus, the CV curves in the third and following cycles were measured at different rates (Fig. 8c and S13a†). The oxidation peak currents, I_p, indicated by the arrows are plotted *versus* the square root of the scan rate, $\nu^{1/2}$, in Fig. 8d. The linear relationship between I_p and $\nu^{1/2}$ suggests a

diffusion-controlled reaction, where the Randles–Sevick relationship given by eqn (4) is applicable:[62]

$$I_p = 0.4463nFAC(nF\nu D/RT)^{1/2} = [269\,000n^{3/2}AD^{1/2}C]\nu^{1/2} \quad (4)$$

where $269\,000n^{3/2}AD^{1/2}C = B$, which can be directly taken from the slope of the linear relationship between I_p and $\nu^{1/2}$ (Fig. 8d). The lithium diffusion coefficients, D_{Li}, thereby determined were 6.05×10^{-13} and 1.54×10^{-12} cm^2 s^{-1} for MCO/CP and MCS/CP, respectively (Table S1†). It is worth noting that the D_{Li} for MCS NSs was about 2.5 times that of the MCO NSs, consistent with the electrochemical performance of the electrodes (Fig. 4). The lithium diffusion coefficient of pristine CP (Fig. S13b and c†), 2.15×10^{-12} cm^2 s^{-1}, was slightly higher than that of MCS/CP, but its very poor electrochemical performance signifies a poor bifunctional catalytic activity of CP in the LOB system.

Conclusion

2D MnCo$_2$S$_4$ nanosheets were grown on carbon paper (MCS/CP) *via* facile, low-cost and environmentally friendly electrodeposition and subsequent vulcanization. The structure, morphology and electrochemical performance of MCS/CP as the oxygen electrode in LOBs were studied and compared with those of the MnCo$_2$O$_4$ nanosheets on CP (MCO/CP). The following are highlighted from this study:

(i) The MCS/CP electrode delivered an initial capacity of 10 760 mA h g^{-1}, twice higher than that of the MCO/CP electrode and 9 times greater than that of CP, 1200 mA h g^{-1}. With an upper limit capacity of 500 mA h g^{-1}, the MCS/CP electrode survived 96 cycles at 200 mA g^{-1}, whereas both the MCO/CP and CP electrodes were stable only for a few cycles.

(ii) The metal sulfide NS catalyst diminished both the ORR and OER overpotentials of CP by 700 mV, while the metal oxide counterpart reduced the overpotential only by 140 mV in total. All in all, the MCS/CP electrode delivered a much higher initial capacity, longer cycling stability, lower overpotentials and a noticeably higher energy efficiency than the MCO/CP electrode, which arose from the efficient bifunctional catalytic activities with ameliorated ORR and OER kinetics.

(iii) The improved electrochemical performances of MCS/CP than MCO/CP are ascribed to a few ameliorating functional features of the former electrode, including the higher electronic conductivity, enhanced ionic diffusivity, mesoporous structure, larger surface area and larger open voids among NSs to accommodate discharge products.

(iv) The electrical conductivity and lithium diffusion coefficient were 400% and 250% higher for the mesoporous MCS/CP than MCO/CP, respectively. The *ex situ* EIS and FESEM analyses performed after 40 cycles revealed better redox kinetics of the MCS/CP electrode because of effective transfer of Li$^+$ ions and electrons across the interface with the electrolyte.

(v) The DOS simulated by the DFT calculations verified a higher electrical conductivity of MCS/CP than MCO/CP due to the metallic characteristic of MCS. The effect of mesoporous metal sulfides on enhanced OER activities was explained by the LiO$_2$ adsorption energy using DFT calculations. The metal sulfide decreased the LiO$_2$ adsorption strength, which in turn improved the cycling stability of MCS/CP.

Author contribution

All experiments were carried out by ZS and the DFT calculations were conducted by JL and FC. The manuscript was written mainly by ZS and JKK. All authors have given approval to the final version of the manuscript.

Conflicts of interest

There are no conflicts to declare.

Acknowledgements

References

1 D. Aurbach, B. D. McCloskey, L. F. Nazar and P. G. Bruce, *Nat. Energy*, 2016, **1**, 16128.
2 Y.-C. Lu, B. M. Gallant, D. G. Kwabi, J. R. Harding, R. R. Mitchell, M. S. Whittingham and Y. Shao-Horn, *Energy Environ. Sci.*, 2013, **6**, 750–768.
3 X. Gao, Y. Chen, L. Johnson and P. G. Bruce, *Nat. Mater.*, 2016, **15**, 882–888.
4 M. V. Reddy, G. V. Subba Rao and B. V. R. Chowdari, *Chem. Rev.*, 2013, **113**, 5364–5457.
5 H. Wang, Q. Gao and L. Jiang, *Small*, 2011, **7**, 2454–2459.
6 T.-Y. Wei, C.-H. Chen, H.-C. Chien, S.-Y. Lu and C.-C. Hu, *Adv. Mater.*, 2010, **22**, 347–351.
7 E. K. Heidari, B. Zhang, M. H. Sohi, A. Ataie and J.-K. Kim, *J. Mater. Chem. A*, 2014, **2**, 8314–8322.
8 X. Wang, C. Yan, A. Sumboja and P. S. Lee, *Nano Energy*, 2014, **3**, 119–126.
9 S. Abouali, M. A. Garakani, Z.-L. Xu and J.-K. Kim, *Carbon*, 2016, **102**, 262–272.
10 M. A. Garakani, S. Abouali, Z.-L. Xu, J. Huang, J.-Q. Huang and J.-K. Kim, *J. Mater. Chem. A*, 2017, **5**, 3547–3557.
11 J. Tang, Y. Ge, J. Shen and M. Ye, *Chem. Commun.*, 2016, **52**, 1509–1512.
12 Y. M. Chen, Z. Li and X. W. D. Lou, *Angew. Chem.*, 2015, **127**, 10667–10670.
13 Q. Liu, J. Jin and J. Zhang, *ACS Appl. Mater. Interfaces*, 2013, **5**, 5002–5008.
14 W. Chen, C. Xia and H. N. Alshareef, *ACS Nano*, 2014, **8**, 9531–9541.
15 S. Liu and S. C. Jun, *J. Power Sources*, 2017, **342**, 629–637.
16 H. Chen, J. Jiang, L. Zhang, H. Wan, T. Qi and D. Xia, *Nanoscale*, 2013, **5**, 8879–8883.
17 M.-K. Han, Y.-S. Jin, B. K. Yu, W. Choi, T.-S. You and S.-J. Kim, *J. Mater. Chem. A*, 2016, **4**, 13859–13865.
18 X. Xu, W. Liu, Y. Kim and J. Cho, *Nano Today*, 2014, **9**, 604–630.
19 Z.-L. Xu, X. Liu, Y. Luo, L. Zhou and J.-K. Kim, *Prog. Mater. Sci.*, 2017, **90**, 1–44.
20 H. Wang, Y. Liang, Y. Li and H. Dai, *Angew. Chem., Int. Ed.*, 2011, **50**, 10969–10972.
21 P. Sennu, M. Christy, V. Aravindan, Y.-G. Lee, K. S. Nahm and Y.-S. Lee, *Chem. Mater.*, 2015, **27**, 5726–5735.
22 Z. Ma, X. Yuan, Z. Zhang, D. Mei, L. Li, Z.-F. Ma, L. Zhang, J. Yang and J. Zhang, *Sci. Rep*, 2015, **5**, 18199.
23 Z. Lyu, J. Zhang, L. Wang, K. Yuan, Y. Luan, P. Xiao and W. Chen, *RSC Adv.*, 2016, **6**, 31739–31743.
24 A. M. Elshahawy, X. Li, H. Zhang, Y. Hu, K. H. Ho, C. Guan and J. Wang, *J. Mater. Chem. A*, 2017, **5**, 7494–7506.
25 S. Sahoo and C. S. Rout, *Electrochim. Acta*, 2016, **220**, 57–66.
26 I. Aldama, V. Barranco, T. A. Centeno, J. Ibañez and J. M. Rojo, *J. Electrochem. Soc.*, 2016, **163**, A758–A765.
27 X. Lu, D. Zheng, T. Zhai, Z. Liu, Y. Huang, S. Xie and Y. Tong, *Energy Environ. Sci.*, 2011, **4**, 2915–2921.

28 J. Huang, B. Zhang, Z. Bai, R. Guo, Z.-L. Xu, Z. Sadighi, L. Qin, T.-Y. Zhang, G. Chen, B. Huang and J.-K. Kim, *Adv. Funct. Mater.*, 2016, **26**, 8290–8299.

29 Z. Sadighi, J. Huang, L. Qin, S. Yao, J. Cui and J.-K. Kim, *J. Power Sources*, 2017, **365**, 134–147.

30 J. Huang, Z. Jin, Z.-L. Xu, L. Qin, H. Huang, Z. Sadighi, S. Yao, J. Cui, B. Huang and J.-K. Kim, *Energy Storage Mater.*, 2017, **8**, 110–118.

31 D. Rathod, S. Warren, K. Keane, D. A. Egan and E. Dempsey, *Anal. Methods*, 2011, **3**, 799–805.

32 K. S. Anuratha, S. Mohan and S. K. Panda, *New J. Chem.*, 2016, **40**, 1785–1791.

33 O. K. Al-Duaij, M. M. Abou-Krisha and M. I. Attia, *Int. J. Electrochem. Sci.*, 2017, **12**, 11972–11986.

34 E. Go, J. Ramirez, E. Valle, *et al.*, *J. Appl. Electrochem.*, 1998, **28**, 71–79.

35 J. Shi, X. Li, G. He, L. Zhang and M. Li, *J. Mater. Chem. A*, 2015, **3**, 20619–20626.

36 J. T. Lee, Y. Zhao, H. Kim, W. Il Cho and G. Yushin, *J. Power Sources*, 2014, **248**, 752–761.

37 X. Lin, L. Zhou, T. Huang and A. Yu, *J. Mater. Chem. A*, 2013, **1**, 1239–1245.

38 Z.-L. Wang, D. Xu, J.-J. Xu, L.-L. Zhang and X.-B. Zhang, *Adv. Funct. Mater.*, 2012, **22**, 3699–3705.

39 C. Tran, X.-Q. Yang and D. Qu, *J. Power Sources*, 2010, **195**, 2057–2063.

40 S. R. Younesi, S. Urbonaite, F. Björefors and K. Edström, *J. Power Sources*, 2011, **196**, 9835–9838.

41 M. Wang, Y. Lai, J. Fang, F. Qin, Z. Zhang, J. Li and K. Zhang, *Catal. Sci. Technol.*, 2016, **6**, 434–437.

42 T. Y. Ma, Y. Zheng, S. Dai, M. Jaroniec and S. Z. Qiao, *J. Mater. Chem. A*, 2014, **2**, 8676–8682.

43 E. Beyreuther, S. Grafström, L. M. Eng, C. Thiele and K. Dörr, *Phys. Rev. B: Condens. Matter*, 2006, **73**, 155425.

44 Q. Li, Z. Xing, D. Wang, X. Sun and X. Yang, *ACS Catal.*, 2016, **6**, 2797–2801.

45 K. Qi, R. Selvaraj, U. Jeong, S. M. Z. Al-Kindy, M. Sillanpää, Y. Kim and C. Tai, *RSC Adv.*, 2015, **5**, 9618–9620.

46 Y.-C. Lu, Z. Xu, H. A. Gasteiger, S. Chen, K. Hamad-Schifferli and Y. Shao-Horn, *J. Am. Chem. Soc.*, 2010, **132**, 12170–12171.

47 N. Imanishi, A. C. Luntz and P. Bruce, *The lithium air battery: fundamentals*, Springer, 2014.

48 H. Wang, Y. Yang, Y. Liang, G. Zheng, Y. Li, Y. Cui and H. Dai, *Energy Environ. Sci.*, 2012, **5**, 7931–7935.

49 X. Lin, Y. Shang, T. Huang and A. Yu, *Nanoscale*, 2014, **6**, 9043–9049.

50 L. Zhou, M. Shao, C. Zhang, J. Zhao, S. He, D. Rao, M. Wei, D. G. Evans and X. Duan, *Adv. Mater*, 2017, **29**, 1604080.

51 S. Yao, J. Cui, Z. Lu, Z.-L. Xu, L. Qin, J. Huang, Z. Sadighi, F. Ciucci and J.-K. Kim, *Adv. Energy Mater.*, 2017, 7(8), 1602149.

52 J. Cui, S. Yao, Z. Lu, J.-Q. Huang, W. G. Chong, F. Ciucci and J.-K. Kim, *Adv. Energy Mater.*, 2018, **8**, 1702488.

53 P. Zhang, Y. Zhao and X. Zhang, *Chem. Soc. Rev.*, 2018, **47**, 2921–3004.

54 X. Zhang, X. Zhang, X.-G. Wang, Z. Xie and Z. Zhou, *J. Mater. Chem. A*, 2016, **4**, 9390–9393.

55 X. Li, Z. Li, X. Yang, L. Jia, Y. Q. Fu, B. Chi, J. Pu and J. Li, *J. Mater. Chem. A*, 2017, **5**, 3320–3329.

56 B. G. Kim, H.-J. Kim, S. Back, K. W. Nam, Y. Jung, Y.-K. Han and J. W. Choi, *Sci. Rep.*, 2014, **4**, 4225.

57 M. M. O. Thotiyl, S. A. Freunberger, Z. Peng, Y. Chen, Z. Liu and P. G. Bruce, *Nat. Mater.*, 2013, **12**, 1050.

58 S. A. Freunberger, Y. Chen, N. E. Drewett, L. J. Hardwick, F. Bardé and P. G. Bruce, *Angew. Chem., Int. Ed.*, 2011, **50**, 8609–8613.

59 N. B. Aetukuri, B. D. McCloskey, J. M. García, L. E. Krupp, V. Viswanathan and A. C. Luntz, *Nat. Chem.*, 2015, **7**, 50–56.

60 B. Horstmann, B. Gallant, R. Mitchell, W. G. Bessler, Y. Shao-Horn and M. Z. Bazant, *J. Phys. Chem. Lett.*, 2013, **4**, 4217–4222.

61 L. Johnson, C. Li, Z. Liu, Y. Chen, S. A. Freunberger, P. C. Ashok, B. B. Praveen, K. Dholakia, J.-M. Tarascon and P. G. Bruce, *Nat. Chem.*, 2014, **6**, 1091–1099.

62 H.-G. Jung, J. Hassoun, J.-B. Park, Y.-K. Sun and B. Scrosati, *Nat. Chem.*, 2012, **4**, 579–585.

63 C. M. Burke, V. Pande, A. Khetan, V. Viswanathan and B. D. McCloskey, *Proc. Natl. Acad. Sci. U. S. A.*, 2015, **112**, 9293–9298.

64 J.-Q. Huang, Z. Wang, Z.-L. Xu, W. G. Chong, X. Qin, X. Wang and J.-K. Kim, *ACS Appl. Mater. Interfaces*, 2016, **8**, 28663–28670.